1 **The catastrophic landfill flowslide at Hongao dumpsite on December 20, 2015 in Shenzhen, China**

2 Qiang Xu[1], Dalei Peng[1], Weile Li[1], Xiujun Dong[1], Wei Hu[1], Minggao Tang[1], Fangzhou Liu[2*]

3 [1]State Key Laboratory of Geohazard Prevention and Geoenvironment Protection, Chengdu University of
4 Technology, Chengdu 610059, China
5 [2]School of Civil and Environmental Engineering, Georgia Institute of Technology, Atlanta, GA, USA

6 **Abstract** A catastrophic flowslide occurred at Hongao dumpsite on Dec 20, 2015 in the Guangming New
7 District of Shenzhen, China. The flowslide caused 73 causalities with 4 missing and damaged 33 buildings.
8 In the absence of extreme weather condition and seismic activity, the causes of the failure were analyzed
9 on the basis of multi-temporal remote sensing images, site investigation, *in-situ* tests, laboratory tests, and
10 numerical analyses. Site investigations showed that the volume of the flowslide deposit was 2.32×10^6 m^3
11 and the volume of dumpsite filling was 6.27×10^6 m^3 at the time of the event, which is 3 times greater than
12 the design capacity. The flowslide was characterized by high travel velocity and long runout distance. The
13 displaced material was primarily silty soil in mixture of construction and demolition waste at high water
14 content (17.3%-42.4%). The primary causes of the failure were concluded as follow: (1) Groundwater flow
15 was stagnated in the dumpsite due to malfunctioned drainage system and the underlying impermeable
16 granite stratum; (2) The accumulation rate and total volume of the waste filling was in exceedance of the
17 design capacity. The failure may be ascribed to the development of excess pore water pressure as evidences
18 of liquefaction were observed at several locations, and it is postulated that such phenomena was related to
19 the surcharge loads imposed by the unregulated disposal activities.

20 **Keywords** Flowslide, Landslide, Municipal Solid Waste (MSW), Dumpsite, Landfill

21 **1 Introduction**

22 Owing to the population growth and industrialization, rapid increase in the accumulation rate of municipal
23 solid waste (MSW) poses challenges in MSW management and urban planning (Huang and Cheng, 2016).
24 As landfilling is the most common method of MSW disposal (Brunner and Fellner, 2007), transforming an
25 abandoned quarry to a dumpsite conserves resources by reclaiming the quarry space and provides MSW
26 storage solution (Zou, 2016). The landfill slope stability is critical to the MSW management, and thus the
27 selection and design of landfills require engineering assessment on both slope stability and environment
28 impact.

29 The porosity and water content of MSW is typically high in an unregulated landfill because of inadequate
30 drainage system, and therefore some failures of MSWs exhibited fluid flow behave, i.e. flowslide, with
31 extremely high mobility (e.g. Dai et al., 2016; Huang and Cheng, 2016). Landfill slope failure in MSW
32 dumpsite can be found in previous studies, wherein 6 reported cases between 1993 and 2005 had resulted
33 in approximately 500 deaths and significant economic loss (Blight, 2008; Blight and Fourie, 2005; Eid et
34 al., 2000; Kjeldsen and Fischer, 1995; Kocasoy and Curi, 1995; Merry et al., 2005; Mitchell et al., 1990).
35 The deadliest event in history killed 278 people in Manila, Philippines in 2000, and the second deadliest
36 event buried 71 houses and killed 143 people on Feb 21, 2005 at Leuwigajah dumpsite near Bandung,
37 Indonesia (Lavigne et al., 2014).

38 Shear strength of MSW is a function of various parameters, including the type and composition of the waste,
39 disposal rate, water content, surcharge, and compaction (Eid et al., 2000; Huvaj-Sarihan and Stark, 2008).
40 The movement of waste failure are complex and still poorly known due to the lack of field monitoring data.
41 Previous studies have focused on empirical methods (e.g. Blight and Fourie 2005; Srour 2011), laboratory
42 experiment, and numerical analyses. An energy balance approach was presented to estimate the maximum
43 flow velocity of MSW slope failure (Blight and Fourie, 2005). The empirical-statistical method still has
44 widespread use in practical applications, but the accuracy is commonly model dependent (Dai et al., 2016;
45 Huang and Cheng, 2016). The mixture of peat, kaolinite, and quartz sand were used in laboratory tests to
46 study the interplay between water content of filling and failure of MSW (Dai et al., 2016). With an increased
47 water content in the MSW, the mobility increases with the maximum and final thickness of deposit decrease.

48 Numerical simulation has been widely used in landfill slope stability analysis (Chang, 2002, 2005; Chugh
49 et al., 2007; Huang and Cheng, 2016), and some of the more advanced methods were recently employed,
50 such as the smoothed Particle Hydrodynamics (SPH) method for runout distance analysis of two typical
51 landfill flow slides occurred in Sarajevo and Bandung (Huang et al., 2013).

52 A MSW landfill consists of mainly construction and demolition waste failed at the Hongao dumpsite in the
53 Guangming New District of Shenzhen, China at approximately 11:40 AM on Dec 20, 2015. The flowslide
54 destroyed 33 buildings and accommodations in the industrial park, and resulted in 74 causalities with 4
55 missing. No extreme weather conditions or seismic activity were reported at the time of the event. This
56 article investigates the characteristics and causes of failure. Field investigation, *in-situ* tests, Unmanned
57 Aerial Vehicle (UAV) stereo-measurements, and remote sensing images were used to analyze the material
58 properties and characteristics of the failure. Laboratory tests and numerical analysis were performed to
59 better understand the failure mechanism.

60 **2 Data and Methodology**

61 A series of satellite images of the site was obtained from Google Earth between Nov 2002 and Feb 2016.
62 Two high resolution pre-/post-failure images were acquired by satellite image and aerial photo. Topography
63 map of the pre-disposal site was provided by the local government, of which the design was submitted by
64 a third-party consulting firm in Dec 2013. Based on the official report on the incident, the design capacity
65 was 4×10^6 m^3 with 9 slope benches at an average ratio of 1:2.5. Field and UAV measurement indicate that
66 the total volume of dumpsite filling was 6.27×10^6 m^3 before failure (5.83×10^6 m^3 by Yin et al., (2016)). The
67 Digital Orthoimage Map (DOM) and Digital Surface Model (DSM) were reconstructed from aerial photos,
68 and a topographic map for the post-sliding dumpsite was generated from the DSM at the scale of 1:1000.
69 Structured terrains in the study site were excavated for vehicles which consisted 9 benches and 3 platforms.
70 Topographic map for the pre-sliding dumpsite was derived by combining the original, pre-sliding, and post-
71 sliding slope images, which also provided an estimation on the volume and depth of the pre-/post-sliding
72 landfill.

73 The preliminary field investigation was conducted on Dec 23, 2015, with a follow-up investigation on Jan
74 21-25, 2016. Field investigations evaluated the topographical, geological, and groundwater conditions.
75 Density, water content, and permeability of the displaced material was measured *in-situ*.

76 Undisturbed and reconstituted soil samples were obtained and used for laboratory tests, including weathered
77 silty soil and waste fillings. Grain size distribution was conducted using wet sieve analysis. Maximum dry
78 density and optimum water content of the displaced material were determined by standard compaction test.
79 The shear parameters of the displaced material (c and ϕ) were obtained by triaxial compression test. In order
80 to back-analyze the failure of dumpsite, input parameters for the material properties and model geometry
81 were measured on site or in the laboratory. The mobilized shear strength was back-calculated using the
82 conventional limit equilibrium method (LEM) to demonstrate the complexity of such progressive failure
83 involving liquefaction and post-failure landslide propagation.

84 **3 Geological and Climatic Setting**

85 The location of the site is shown in Fig. 1a, of which the pre-failure image was obtained by Pleiades image
86 on Dec 18, 2015 (2 days before failure) and the post-failure aerial image was taken by UAV (3 days after
87 failure) as shown in Fig. 1b and 1c. The dumpsite was located 23 km north of Shenzhen and 5 km south of
88 the Guangming New District (E113°56'5", N22°42'44"). The dumpsite was surrounded by three ridges with
89 a free face excavated in a mild slope gradient. The bedrock of the dumpsite is mainly Cretaceous granite
90 rock (Fig. 2a and 2b). The landfill consisted of construction waste with silty soil, clay, rock, and gravel (Fig.
91 2 and 3).
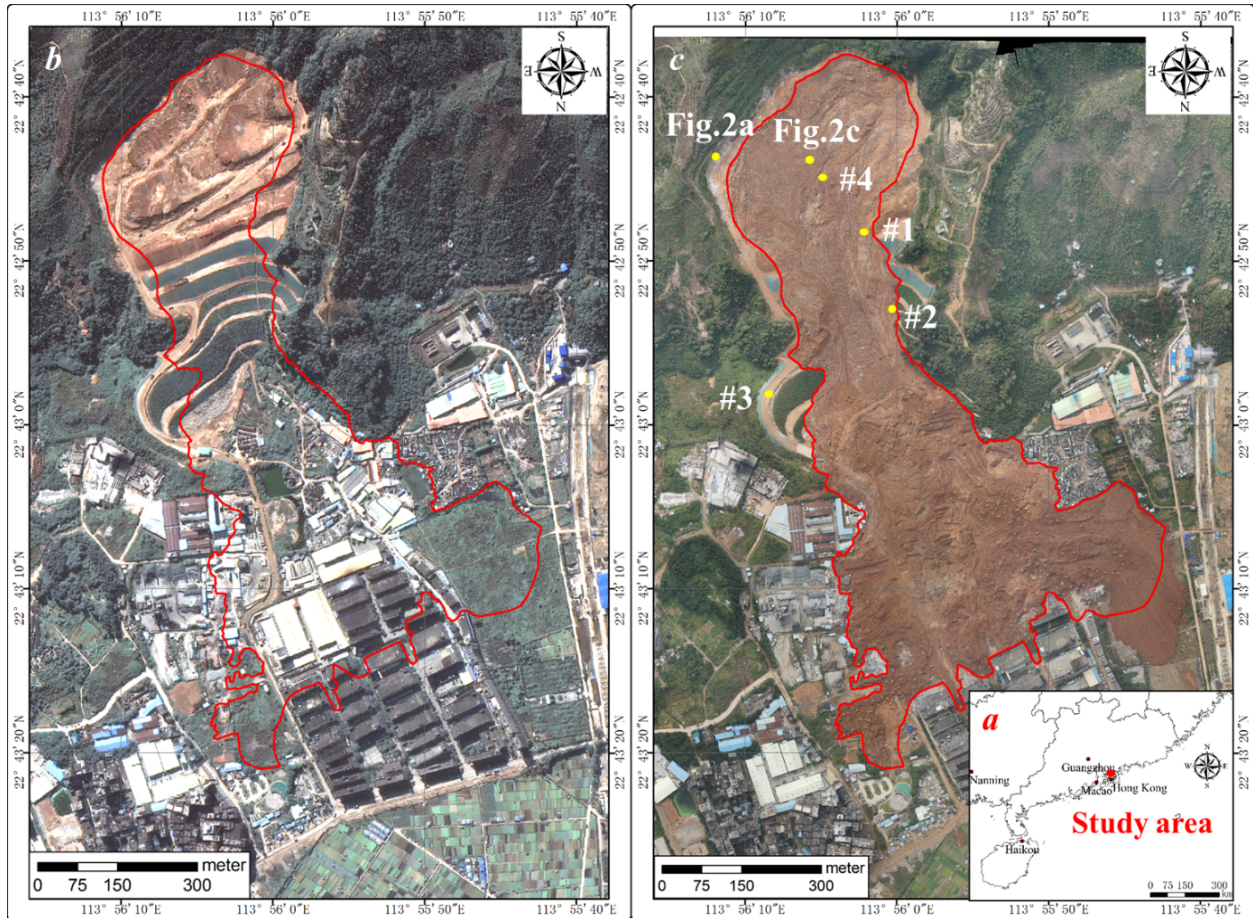
Fig. 1 Location of the study site and images of the pre-/post-failure dumpsite. The boundary of the flowslide is indicated in red. **a** Location of the study area; **b** Pleiades satellite image (Dec 18, 2015); **c** Aerial photo of the flowslide with locations of samples for laboratory test (Dec 23, 2015).

The study area belongs to the zone of subtropical monsoon climate with an average temperature of 22° and an average annual precipitation of 1500 mm concentrating between April and September (> 85 % of the annual rainfall) (Zhang et al., 2006). Based on the rainfall data from the nearby Tangjia Rainfall Station (Jan 1, 2013 - Dec 20, 2015) as shown in Fig. 4, a heavy rainfall occurred on Dec 9, 2015 with accumulated precipitation of 67.8 mm. The area of catchment (Fig. 5a) was estimated as 4.7×10^5 m^2, which was nearly 3 times greater than the area of the dumpsite (1.6×10^5 m^2). Drainage system was implemented to collect surface run-off by the drainage pipes installed at a higher elevation above the dumpsite and diverted into the peripheral drainage channels. Field evidences suggested that the drainage system was abandoned, possibly due to the lack of maintenance (Fig. 5b and 5c). With the inadequate drainage, ingress of rainwater in the dumpsite was permitted (Fig. 6c), in addition to the concentration of surface run-off and groundwater into the dumpsite. The infiltration rate of the waste filling was estimated as 5.26×10^{-6} cm/s by field double ring infiltrometer. Low permeability and inadequate drainage resulted in high water content and high pore water pressure in the dumpsite. The groundwater in the study area were mainly bedrock fissure water and Quaternary pore water (Fig. 6).

110

111 Fig. 2 Photos of the rock and soil specimen collected from the displaced material. **a** Exposed granite rock
112 near the flowslide scarp; **b** Close view of the granite rocks; **c** Displaced material in the zone of depletion;
113 **d** Materials in the flowslide source area.
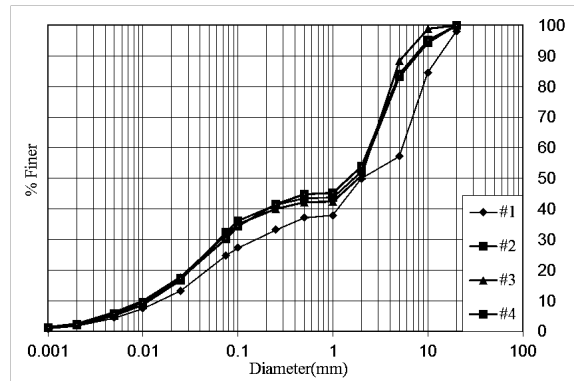
114

115 Fig. 3 Particle size distribution of the waste filling (with sieve sizes of 20, 10, 5, 2.0, 1, 0.5, 0.25, 0.10,
116 0.075, 0.025, 0.01, 0.005, 0.002, and 0.001 mm)
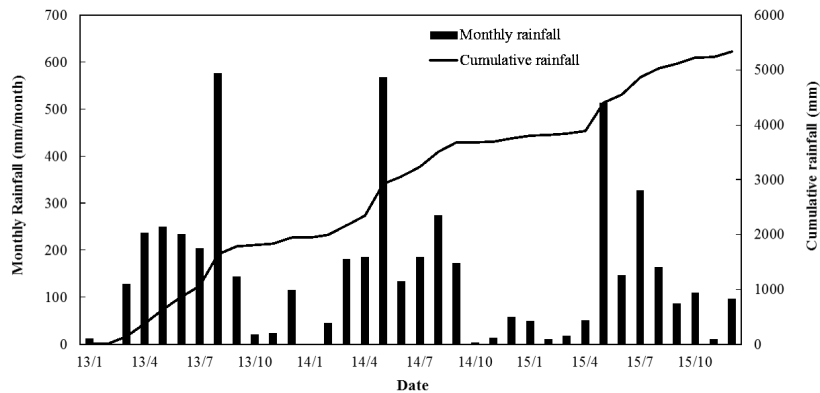
117

118 Fig. 4 Monthly rainfall and cumulative precipitation between 2013 and Dec 2015.

119

Fig. 5 **a** An overview of the catchment area (Google Earth image); **b** The surrounding peripheral drainage
channel of the dumpsite was abandoned; **c** Damaged drainage pipes were not repaired and failed to divert
surface run-off into the peripheral drainage channel. Surface run-off concentrated in the waste filling.

123
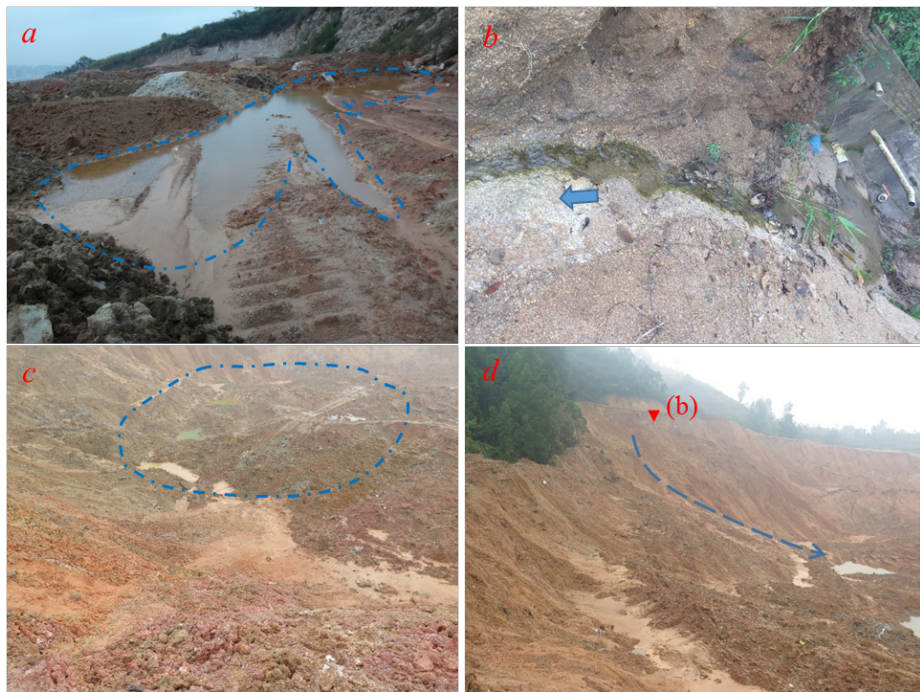
Fig. 6 **a** Groundwater overflow in the rock fissures near the flowslide crown; **b** Water accumulation in the
flowslide crown; **c** Water accumulation in the source area; **d** Surface run-off and infiltration contributed to
groundwater seepage.

4 Multi-Temporal Remote Sensing Images

The development of dumpsite and landform changes are presented by a series remote sensing images taken between 2002 and 2016 (Fig. 7). It is postulated that the quarry was active between 2002 and 2008. However, formation of ponds of various sizes at different spatial and temporal locations in the quarry indicated low permeability and the lack of drainage network (Fig. 7b, 7c, and 7d). The quarry was abandoned in or before 2008 as shown in Fig. 7c (Feb 20, 2008) with a small amount of waste filling in the pit. A large-scale pond was later formed due to groundwater and rainfall accumulation (Fig. 7d). The depth of the pit was over 100 m before the routine disposal activities. A service road was excavated between two rock hills exiting the quarry and formed a small-scale gully cross the pit longitudinally (Fig. 7a, 7b, 7c, and 7d). Additionally, a small-scale platform (the office area of the abandoned quarry) was excavated at the immediate downstream of the quarry exit. The gully was covered by the construction of a multi-benched retaining slope between the rock hills as waste disposal continued throughout the process (Fig. 7e). Disposal activity started possibly in 2014 (Fig. 7e and 7f), and the accumulation rate of the waste filling was considerably fast (Zou, 2016).

An unpaved road was excavated on the east of the quarry connecting the crest and toe of the hillslope as shown in Fig. 7e. A large number of trucks can be seen transporting waste filling to the dumpsite. A large amount of construction waste was dumped in the pit with 4 slope benches built at the exit of the pit (Fig. 7e). The volume of the waste increased significantly with the 1st and 2nd benches completed in late 2014, and the 3rd to 4th benches were still under construction until Jan 2015 (Fig. 7f).

The rapid accumulation and the total volume of the waste filling received some attentions before failure. An environmental assessment provided by a third-party consulting firm warned the erosion at the site and its influence on the slope stability in Jan 2015 (Zou, 2016). The disposal activity was ceased for a while as no trucks were seen in the image (Fig. 7f), and it was verified by the interview with the local inhabitants. The disposal activity was resumed in or before April 2015, and the 4th bench was completed by then (Fig. 7g). By comparing Fig. 7g and Fig. 7h, significant modifications on the landform occurred with a major increase in the volume of the waste filling as the landfill was close to the crest of the pit. The waste filling appeared flattened and disposal activity was intense as more than 20 trucks were found in Fig. 7h. A total of 8 slope benches were completed with surface drainage channels installed on the hillslope, and the 9th bench was still under construction before failure. The thickness of the waste filling was around 90 m with a volume of $6.3 \times 10^6 \, m^3$ (Fig. 8a) by extracting the difference between the pre- and post-filling DEMs.

156
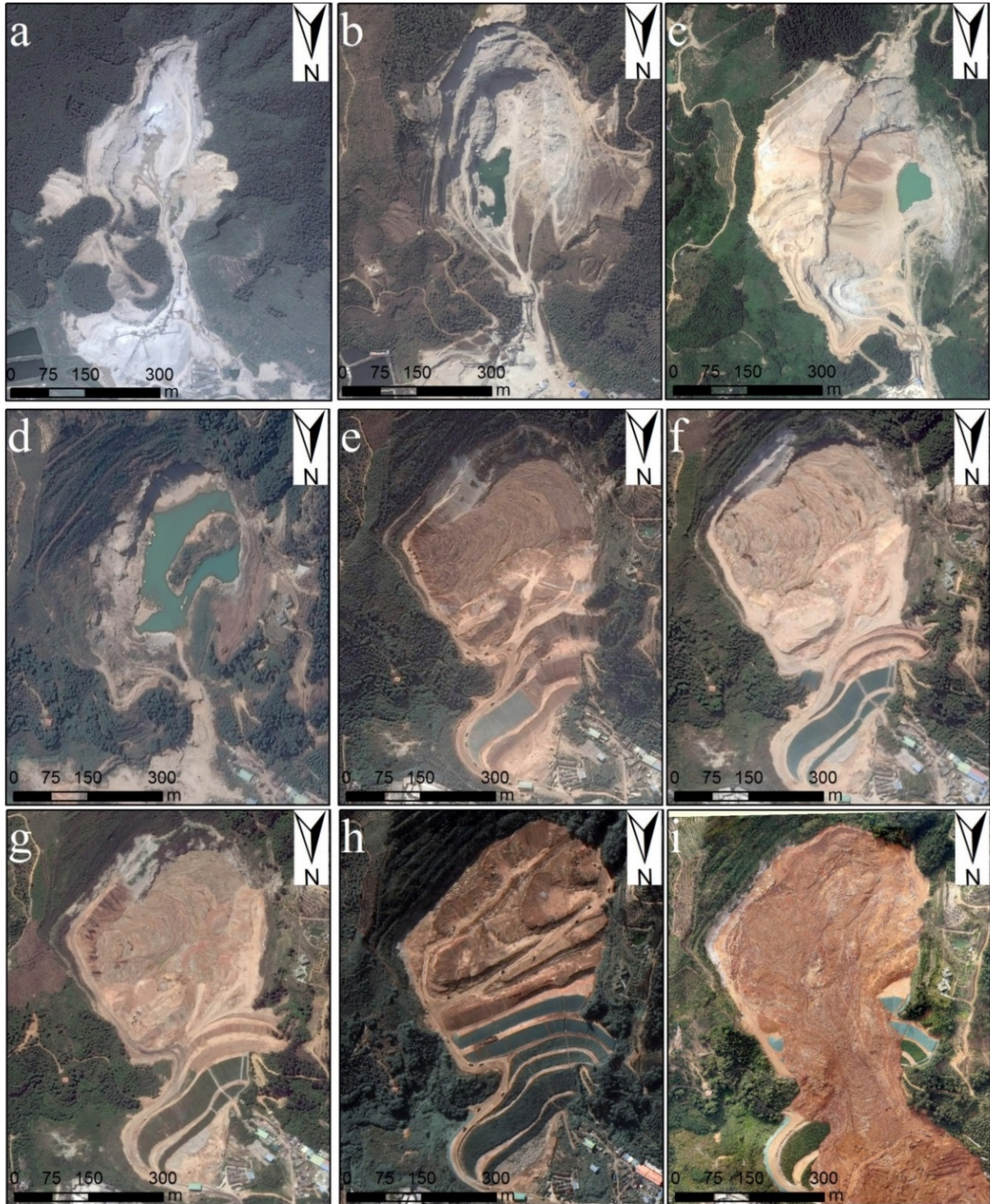
Fig. 7 Multi-temporal remote sensing images of the study area. **a** 08/31/2002; **b** 02/20/2008; **c** 08/30/2010; **d** 11/25/2013; **e** 11/17/2014; **f** 01/23/2015; **g** 04/14/2015; **h** Pleiades (12/18/2015); **f** Aerial (12/23/2015). Image **a** to **g** were obtained from Google Earth. A service road was excavated at the exit of the quarry with a width of nearly 70 m (see image **a**, **b**, **c**, and **d**).
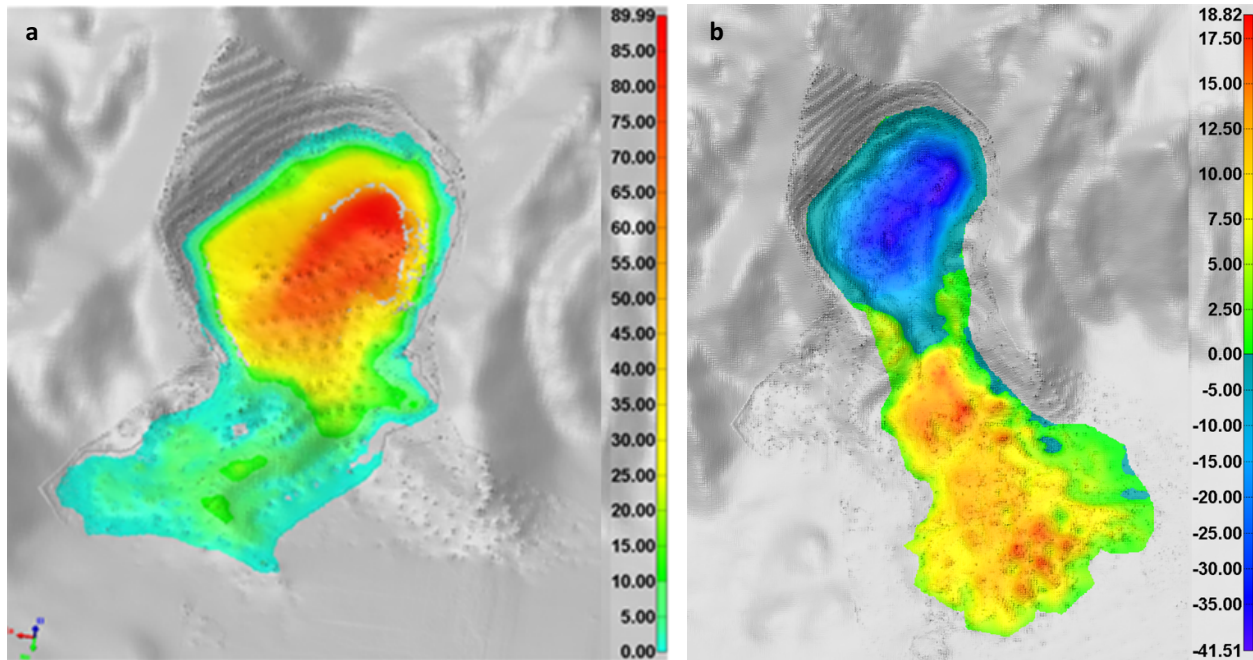
161

162 Fig. 8 **a** The thickness distribution of the dumpsite based on the pre-/post-disposal DEMs; **b** The elevation
163 variations of the dumpsite estimated between the pre-/post-sliding DEMs.

164 **5 Flowslide Characteristics**

165 The flowslide area can be divided into the source area and the flow-accumulation area as shown in Fig. 9.
166 The source area was the abandoned quarry pit. The mass slid in the direction of 340° with the maximum
167 traveling distance of 1203 m. The maximum thickness of the remaining material in the source area was
168 41.51 m with an average of 20.5 m (Fig. 9 and Fig. 10). The maximum deposit thickness in the flow-
169 accumulation area was 18.2 m with an average of 8.21 m (Fig. 8b). The geometry of a flowslide can be
170 expressed in length (L), height (H), width (W), and area (S) (Legros, 2002; Scheidegger, 1973). The
171 geometric parameters are indicated in the simplified flowslide geometry in Fig. 11 with values tabulated in
172 Table 1, Table 2 and Table 3.
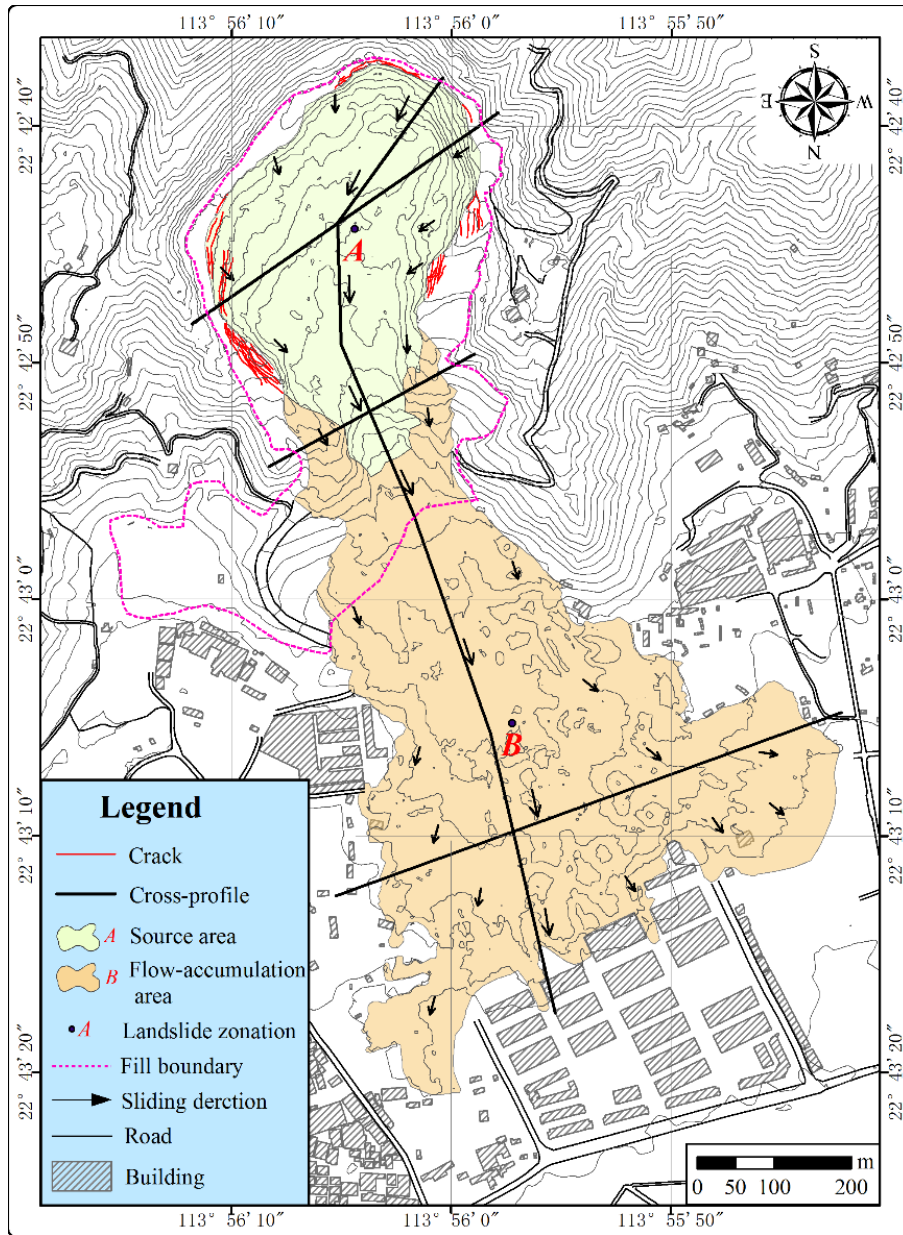
173

174 Fig. 9 The topographic map of the flowslide.
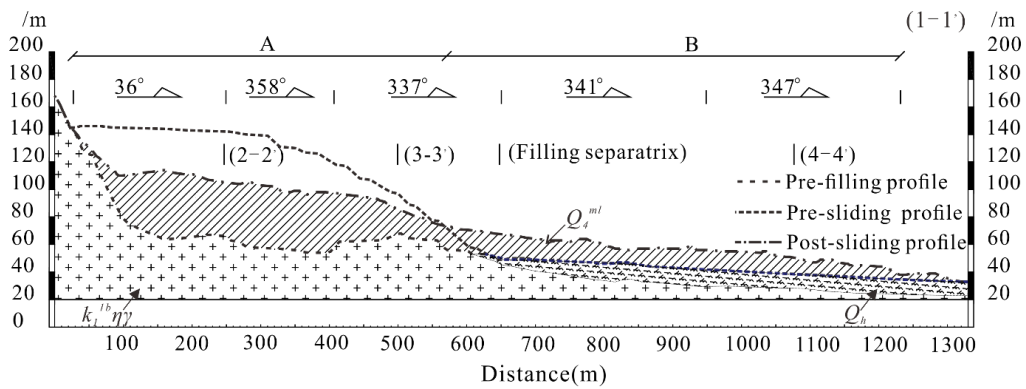
175

176 Fig. 10 The geological and topographical cross section (profile line 1-1')
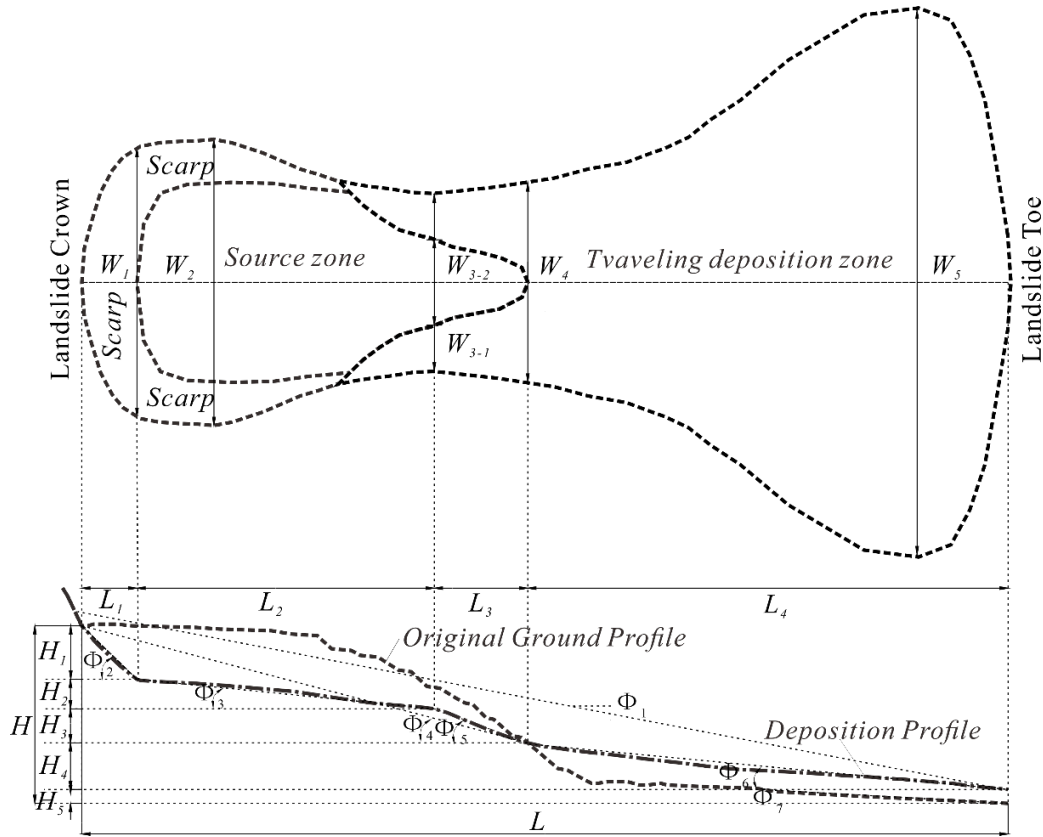
177

178 Fig. 11 Simplified illustration of the flowslide geometry. L: runout distance; H: elevation; W_1: scarp width;
179 W_2: max width of the source area; W_3: frontal width of the source area; W_4: width of the shear crack; W_5:
180 max width of the flow-accumulation area; L_1: horizontal length of the scarp; L_2: horizontal length of the
181 mild slope; L_3: horizontal length of the steep slope; L_4: horizontal length of the flow-accumulation area; H_1:
182 height of the scarp; H_2: height of the mild slope; H_3: height of the steep slope; H_4: height of the flow-
183 accumulation area; H_5: thickness of the toe of the flowslide; Φ_1: extension angle; Φ_2: slope gradient of the
184 scarp; Φ_3: mild slope gradient; Φ_4: slope gradient of the source area; Φ_5: steep slope gradient; Φ_6: slope
185 gradient of the flow-accumulation area; Φ_7: slope gradient of the foundation area

186

Table 1 Geometric parameters of the flowslide (Length and Width)

Parameter	L (m)	H (m)	W_1 (m)	W_2 (m)	W_{3-1} (m)	W_{3-2} (m)	W_{4-1} (m)	W_{4-2} (m)	W_5 (m)
Value	1204.67	111.31	212.5	399.32	218.31	149.38	217.71	64.63	592.25

187

Table 2 Geometric parameters of the flowslide (Angle)

Parameter	Φ_1 (°)	Φ_2 (°)	Φ_3 (°)	Φ_4 (°)	Φ_5 (°)	Φ_6 (°)	Φ_7 (°)	K	S (m^2)
Value	5.28	28.06	1.2	7.62	11.36	3.08	1.36	0.32	398619.6

188

Table 3 Geometric parameters of the flowslide (Area and Thickness)

Parameter	Area A	Area B
S (m^2)	11.35×10^4	28.51×10^4
V (m^3)	3.95×10^6 (remaining)	2.34×10^6
T_{max} (m)	41.51	18.82
T_{ave} (m)	20.49	8.21

5.1 Source Area

The source area of the flowslide is the quarry pit with a length (L_{1+2+3}) of 540.30 m and a width (W_2) of 399.32 m. The area of the source area (S_A) is 11.35×10^4 m^2 and the height (H_{1+2+3}) was 68.5 m with an apparent dip (Φ_4) of 7.62° (Fig. 12 and Table 1). The volume of the mobilized material from the source area was 2.32×10^6 m^3 and the remaining volume was 3.95×10^6 m^3. The maximum thickness of the source area (T_{A-max}) was 41.5 m with an average thickness (T_{A-ave}) of 20.5 m. The west of the main scarp has steep slope gradient with a mild gradient on the east. The height of the steep scarp was 25-47 m, while the height of the mild scarp was 10-20 m. The geological cross section (profile line 2-2') is shown in Fig. 12c. The maximum thickness of the source area was 40.65 m with an average of 34.83 m. The overview of the source area and surface cracks are shown in Fig. 12a and 12b, respectively.
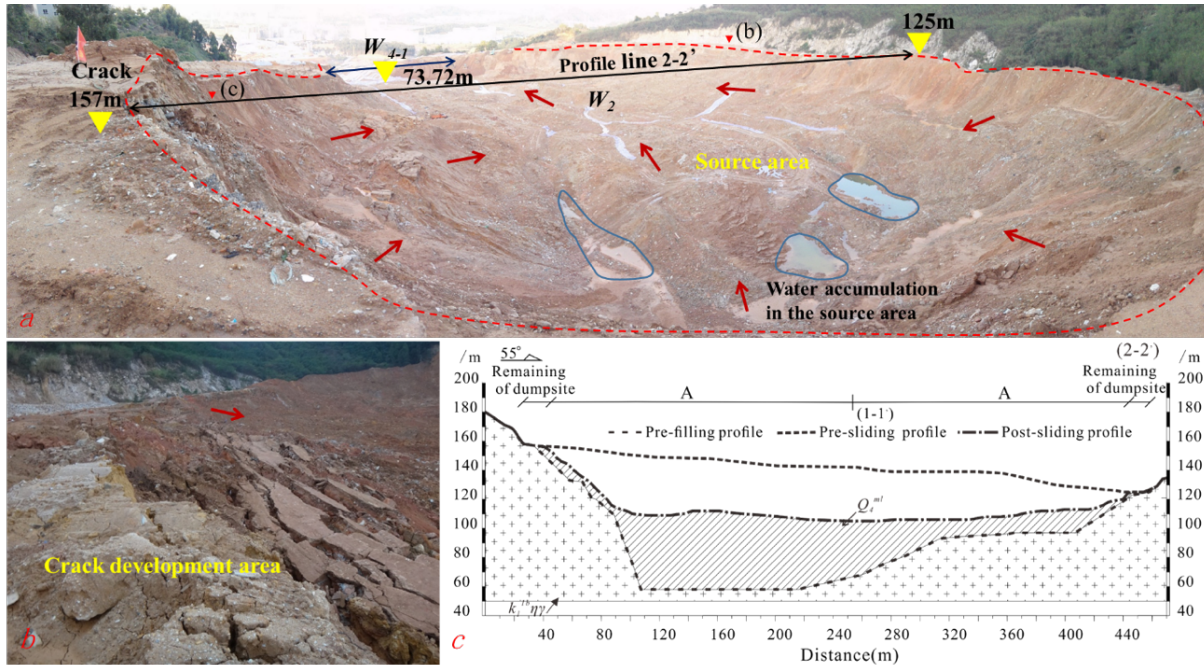
Fig. 12 **a** An overview of the source area (image taken at the flowslide crown facing north). A large opening (W_{4-1}) formed due to the failure of the retaining slope (the exit of the original quarry pit), which provided passage for the flowslide and permitted rapid release of kinematic energy; **b** Surface cracks were developed due to unloading near the crest and the flanks of the flowslide; **c** The geological cross section (profile line 2-2') of the source area.

Pore water pressure increases as rainwater and groundwater ingress in the dumpsite. The lack of drainage resulted in waste filling saturation in the basal zone of the dumpsite which appeared as the final sliding bed of the flowslide (Fig. 12a). A large amount of silty soil was observed in the source area. The water content of the remaining materials in the source area is 17.3%-42.4% (6 sampling locations). The materials on both sides of the source area were mobilized due to the debuttressing effect as the waste filling in the lower portion of the dumpsite slid into the downstream industrial park, and in consequence, caused collapse of the dumpsite. Step-like steep scarp was formed on the west of the main scarp with tensile cracks developed on the rear edge as well as both sides of the scarp.

The presence of the aforementioned rock ridges formed unfavorable topography for the stability of the retaining slope as it promoted a narrow gully for groundwater flow (Fig. 7c and Fig. 9). As a result of the retaining slope failure, a large opening was formed at the elevation of 73.7 m (between the front edge of the steep scarp and the rear edge of the flow-accumulation area) as shown in Fig. 9, Fig. 10, and Fig. 12a. The displaced material was stratified in the middle part of the flow-accumulation area during the high-speed sliding. The shape of the failed retaining slope was half-elliptic-like with a width (W_{4-1}) of 217.7 m and a

219   height (H_b) of 27.5 m (Fig. 13a and 13c).
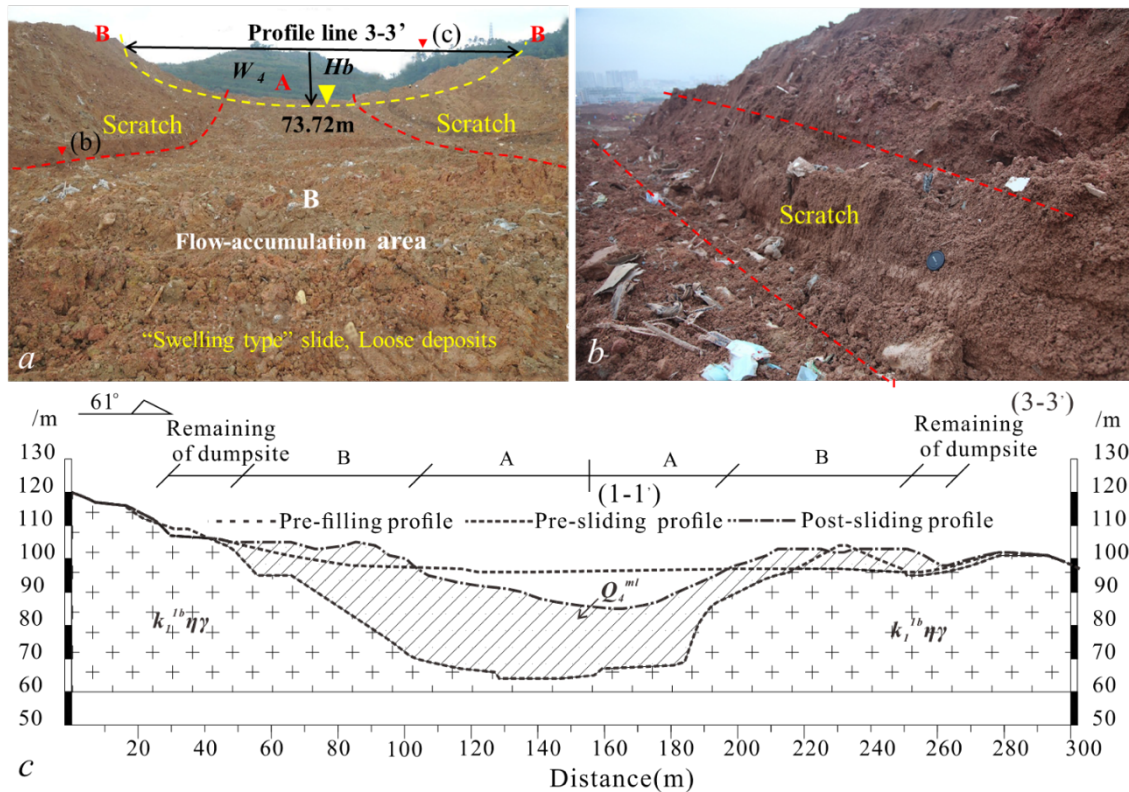
220
221   Fig. 13 **a** The half-elliptic-like opening of the failed retaining slope; **b** Details on the scratch caused by the
222   mass movement; **c** Geological cross section (profile line 3-3') of the failed retaining slope located at the
223   original quarry pit between the two rock hills.

224   **5.2 Flow-Accumulation Area**

225   The fan-shaped flow-accumulation area mantled the retaining slope of the dumpsite as well as a large part
226   of the industrial park as shown in Fig. 12a. The water content of the displaced material was 32.1%-37.2%
227   (3 sampling locations). The original slope gradient of the industrial park (Φ) was 1.36° along the profile
228   line 1-1' as shown in Fig. 12 and Table 1. The area located immediately downstream of the dumpsite was
229   relatively flat with no major construction except a pond (area approx. 3600 m^2) and a channel (width: 7 m
230   and length: 130 m). Most of the industrial structures were located on the east, west, and north side of the
231   pond as shown in Fig. 9, and thus created an ideal flow channel for the flowslide. The failure of the rock
232   retaining slope resulted in an opening for the waste fill movement which subsequently destroyed
233   downstream buildings (Fig. 14 and 15).

234
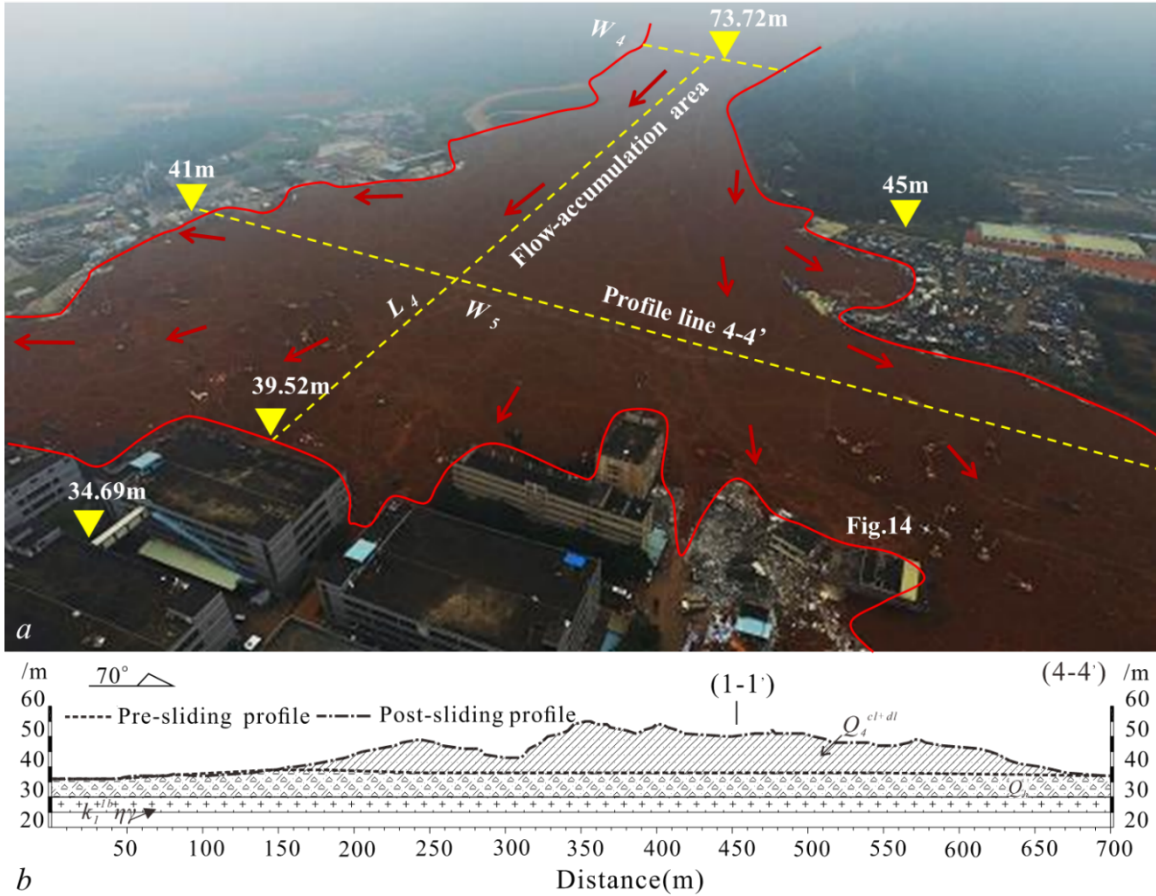
235 Fig. 14 **a** The overview of the flow-accumulation area with elevations (China News Agency); **b** Geological
236 cross section (profile line 4-4') of the flow-accumulation area. The length (L_4) was 664.4 m and the width
237 (W_3) was 218.3 m with the width of the front edge (W_5) of 592.3 m. The area of the flow-accumulation area
238 is 28.51×10^4 m^2, and the elevation difference (H_4) was 35.7 m with an apparent dip (Φ_6) of 3.08°. The
239 average thickness in the flow-accumulation area was 8.21 m with the maximum thickness of 18.82 m (Fig.
240 12c, Table 1, and Table 3).

241
242 Fig. 15 The damage of buildings in the industrial park (China News Agency)

6 Back-Analyses of the Flowslide

6.1 Flowslide Movement

The high sliding velocity and long-runout distance of the flowslide may be related to a more diffuse failure due to liquefaction near the base of the slope. Evidences of localized liquefaction can be found at several locations (Fig. 16). Empirical correlation was used to back-calculate the flowslide travel velocity on the basis of its geometrical characteristics. Laboratory tests and numerical analyses were performed to better understand the failure process.

Fig. 16 Evidences of liquefaction near the opening of the failed slope.

The source area of the flowslide was in the elevation of 142 m and the horizontal runout distance (L) was approximately 1203 m with an elevation difference (H) of 111 m (Fig. 11). The velocity of a high-speed landslide can be estimated by $v = \sqrt{2g \times (H - f \times L)}$ (Scheidegger, 1973), where v is the sliding velocity (m/s), g is the gravitational acceleration (m/s^2), H and L are the elevation difference and horizontal distance (m) between the crown and toe of the flowslide, respectively. f is the equivalent friction coefficient referred as the ratio of height and runout distance of the flowslide (f = H/L). The equivalent friction coefficient of the flowslide was 0.092. The sliding velocity was back-calculated and presented in Fig. 17.
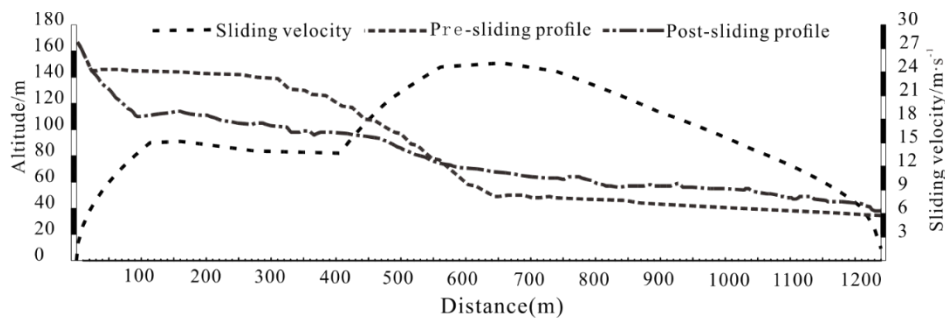
Fig. 17 The relationship between sliding velocity along profile line 1-1' and pre-/post-sliding landform.

Based on the back-calculated velocity profile, two sharp increases were identified, including the initiation of the waste filling near the steep scarp and the acceleration of the flowslide when exiting the dumpsite. The sliding velocity was increased to 15.17 m/s as waste filling reached the bottom of the steep scarp. The velocity displaced material gradually decreased to approximately 13 m/s before accelerate to the maximum velocity of 25.15 m/s as it reached the opening of the quarry. The second sharp acceleration was followed by the rapid dissipation of kinematic energy and reduction in velocity after reaching the flow-accumulation area (elev. 50 m). It was estimated that the sliding velocity was reduced to 15.68 m/s when it made contact with the downstream buildings, and then ceased moving due to the obstruction. The geometry and velocity exhibited clear characteristics associated with high-speed long-runout flowslides.

6.2 Numerical Analyses

Basic material properties were obtained from *in-situ* and laboratory tests. Dry density of the waste filling was 1.25-1.48 g/cm^3 with a void ratio of 0.83-1.31. Standard compaction tests suggested that the optimal water content of 15.3% with highest dry density of 1.79 g/cm^3. The surface of the filling was in loose state with the degree of compaction of 69.8%-82.7%. Based on the undrained shear test, the c and ϕ of the filling were 4.7 kPa and 31.9°, respectively, and thus the friction angle was considerably higher than the gradient of the slope. No strain-softening was observed in the saturated specimen under triaxial tests.

Numerical simulation for diffuse failure involves liquefaction and post-failure propagation is challenging (Take and Beddoe, 2014), and the conventional LEB is typically not applicable for analyzing propagation of landslide originating from diffuse failure induced by liquefaction (Cascini et al., 2009, 2013). Back-analyses was performed using SLOPE/W with Morgenstern Prince Limit Equilibrium Analysis under the assumption of a fully saturated basal zone in the dumpsite before failure. The back-analyses using LEB method typically set the FoS to unity for back-calculating the mobilized strength. The final sliding surface and a hypothetic groundwater level were added to determine the shear strength in an iterative approach with estimated dry density of filling of 1.65 g/cm^3 (Fig. 18), however the back-calculated friction angle was significantly less than the experimental result.
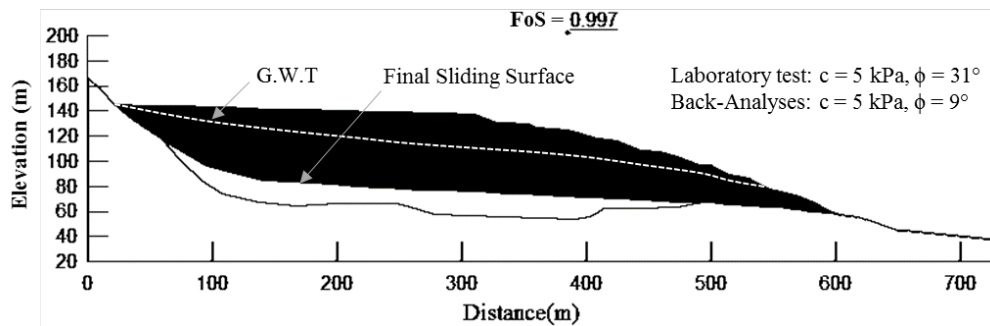
Fig. 18 Back-calculated mobilized strength by using 2D numerical model with LEM.

The implausible mobilized strength shows that back-analyses using LEB is not applicable to the flowslide, as the failure may involve liquefaction with subsequent progressive failure and post-failure propagation. Notwithstanding the complex progressive mechanism and over-simplified force equilibrium method, the misleading results of the back-analyses can be directly ascribe to the misuse of static pre-shearing pore-water pressure with measured final sliding surface. Such erroneous back-analyses strategy was discussed in detail by Take et al., (2004). It was postulated that the failure may be initiated at a relatively shallow depth near the base of the slope as a result of static liquefaction, and followed by progressive backward mobilization of the fillings in the dumpsite.

The exact reason of excess pore water pressure remains unclear but it was a key factor in causing the failure (Ouyang et al., 2016). The excess pore water pressure can be induced by: (1) rapid surcharge on the dumpsite while pore water pressure cannot dissipate sufficiently fast, and/or (2) the waste filling was loosely packed with large pores in the mesco-structure, and the collapse of the structure lead to the shrinkage of pores, which resulted in the excess pore water pressure. Since the permeability of the waste filling was considerably low, it may result in saturation in the basal zone of the waste filling. As no clear drainage passage were found in the filling, the displaced material may remain undrained 'at failure'.

7 Conclusion

The Hongao dumpsite failure is of direct interest to the scientific community due to its complex progressive failure mechanism and significant societal impact. The flowslide was investigated here to better understand its characteristics and mechanism. The flowslide is divided into the source area and the flow-accumulation area. The volume of the source area was 2.32×10^4 m^3 with the average thickness of 20.5 m (max. 41.5 m).

308   The volume of the fan-shaped flow-accumulating area was 2.34×10^6 m^3 with the average thickness of 8.2
309   m (max. 18.8 m). The volume expansion coefficient of the flowslide was 1.007. The maximum sliding
310   velocity of the flowslide was 25.15 m/s at the opening of the dumpsite, and reduced to 15.68 m/s as it
311   reached the industrial park and ceased moving due to the obstruction of buildings.

312   The flowslide was characterized by high-speed and long runout distance, which may be related to the (1)
313   suitable topography with a height of 124 m between the crown and toe with large potential energy needed
314   for high-speed and long runout flowslide, and (2) the low permeability and lack of drainage in the waste
315   filling in the dumpsite with impermeable bedrock resulted in groundwater stagnation, and thus high pore-
316   water pressure. Additionally, the volume of the waste filling was estimated as 6.27×10^6 m^3, which was three
317   times larger than the design capacity of the dumpsite. The failure of the retaining slope constructed between
318   two bedrock ridges formed a narrow opening for the flowslide, which facilitated the sudden release of
319   kinematic energy generating high sliding velocity and long travel distance.

320   The failure mechanism remains unclear yet it was clear that a more diffuse failure occurred with liquefaction
321   and post-failure propagation of the flowslide. The inapplicability of the LEM demonstrated the complexity
322   of the mechanism by yield erroneous mobilized strength, which also indicates the predicament of simulating
323   liquefaction-induced slope failures with conventional numerical approaches. The cause(s) of excess pore-
324   water pressure is not clear, but the unregularly disposal activities in addition to the ingress of rainwater and
325   high pore water pressure played important roles in deformation of the dumpsite. Although the flowslide
326   destruction process was fast with excessive deposits, it is postulated that signs of deformation may have
327   already appeared in the study site but not discovered due to the absence of field monitoring. Further analysis
328   is undergoing at SKLGP to assess the cause(s) involved for generating the excess pore water pressure.

329   **Acknowledgments** Authors are indebted to Dr. J. David Frost for his constant support on the collaboration.
330   The work was financially supported by the NSFC (Grant No. 41521002) and the National State Key 973
331   Project (Grant No. 2014CB744703) from the Ministry of Science and Technology of the People's Republic
332   of China.

333   **Reference**

334   Blight, G.: Slope failures in municipal solid waste dumps and landfills: a review, Waste Manag. Res.,
335   26(5), 448–463, doi:10.1177/0734242X07087975, 2008.
336   Blight, G. E. and Fourie, A. B.: Catastrophe revisited–disastrous flow failures of mine and municipal
337   solid waste, Geotech. Geol. Eng., 23(3), 219–248, 2005.
338   Brunner, P. H. and Fellner, J.: Setting priorities for waste management strategies in developing countries,
339   Waste Manag. Res., 25(3), 234–240, doi:10.1177/0734242X07078296, 2007.
340   Cascini, L., Cuomo, S., Pastor, M. and Sorbino, G.: Modeling of rainfall-induced shallow landslides of
341   the flow-type, J. Geotech. Geoenvironmental Eng., 136(1), 85–98, 2009.
342   Cascini, L., Cuomo, S., Pastor, M. and Sacco, C.: Modelling the post-failure stage of rainfall-induced
343   landslides of the flow type, Can. Geotech. J., 50(9), 924–934, 2013.
344   Chang, M.: A 3D slope stability analysis method assuming parallel lines of intersection and differential
345   straining of block contacts, Can. Geotech. J., 39(4), 799–811, doi:10.1139/t02-020, 2002.
346   Chang, M.: Three-dimensional stability analysis of the Kettleman Hills landfill slope failure based on
347   observed sliding-block mechanism, Comput. Geotech., 32(8), 587–599, 2005.
348   Chugh, A. K., Stark, T. D. and DeJong, K. a: Reanalysis of a municipal landfill slope failure near
349   Cincinnati, Ohio, USA, Can. Geotech. J., 44(1), 33–53, doi:10.1139/t06-089, 2007.
350   Dai, Z., Huang, Y., Jiang, F. and Huang, M.: Modeling the flow behavior of a simulated municipal solid
351   waste, Bull. Eng. Geol. Environ., 75(1), 275–291, doi:10.1007/s10064-015-0735-8, 2016.
352   Eid, H. T., Stark, T. D., Evans, W. D. and Sherry, P. E.: Municipal solid waste slope failure. I: Waste and
353   foundation soil properties, J. Geotech. Geoenvironmental Eng., 126(5), 397–407, 2000.
354   Huang, Y. and Cheng, H.: A simplified analytical model for run-out prediction of flow slides in municipal
355   solid waste landfills, Landslides, 1–9, doi:10.1007/s10346-016-0688-4, 2016.

356 Huang, Y., Dai, Z., Zhang, W. and Huang, M.: SPH-based numerical simulations of flow slides in
357 municipal solid waste landfills., Waste Manag. Res., 31(3), 256–64, doi:10.1177/0734242X12470205,
358 2013.
359 Huvaj-Sarihan, N. and Stark, T. D.: Back-Analyses of Landfill Slope Failures, 6th Int. Conf. Case Hist.
360 Geotech. Eng., (2), 1–7, 2008.
361 Kjeldsen, P. and Fischer, E. V: Landfill gas migration - field investigations at Skellingsted landfill,
362 Denmark, Waste Manag. Res., 13(5), 467–484, 1995.
363 Kocasoy, G. and Curi, K.: The Ümraniye-Hekimbaşi open dump accident, Waste Manag. Res., 13(4),
364 305–314, 1995.
365 Lavigne, F., Wassmer, P., Gomez, C., Davies, T. A., Sri Hadmoko, D., Iskandarsyah, T. Y. W. M.,
366 Gaillard, J., Fort, M., Texier, P., Boun Heng, M. and Pratomo, I.: The 21 February 2005, catastrophic
367 waste avalanche at Leuwigajah dumpsite, Bandung, Indonesia, Geoenvironmental Disasters, 1(1), 1–12,
368 doi:10.1186/s40677-014-0010-5, 2014.
369 Legros, F.: The mobility of long-runout landslides, Eng. Geol., 63, 301–331 [online] Available from:
370 http://www.sciencedirect.com/science/article/pii/S0013795201000904 (Accessed 25 June 2014), 2002.
371 Merry, S. M., Kavazanjian Jr, E. and Fritz, W. U.: Reconnaissance of the July 10, 2000, Payatas landfill
372 failure, J. Perform. Constr. Facil., 19(2), 100–107, 2005.
373 Mitchell, J. K., Seed, R. B. and Seed, H. B.: Kettleman Hills waste landfill slope failure. I: Liner-system
374 properties, J. Geotech. Eng., 116(4), 647–668, doi:10.1061/(ASCE)0733-9410(1990)116:4(647), 1990.
375 Ouyang, C., Zhou, K., Xu, Q., Yin, J., Peng, D., Wang, D. and Li, W.: Dynamic analysis and numerical
376 modeling of the 2015 catastrophic landslide of the construction waste landfill at Guangming, Shenzhen,
377 China, Landslides, 2016(April), doi:10.1007/s10346-016-0764-9, 2016.
378 Scheidegger, A. E.: On the prediction of the reach and velocity of catastrophic landslides, Rock Mech.
379 Rock Eng., 5(4), 231–236, doi:10.1007/BF01301796, 1973.
380 Srour, G.: Mine waste failure: an analysis of empirical and graphical runout prediction methods,
381 University of British Columbia., 2011.
382 Take, W. A. and Beddoe, R. A.: Base liquefaction: a mechanism for shear-induced failure of loose
383 granular slopes, Can. Geotech. J., 51(5), 496–507, doi:10.1139/cgj-2012-0457, 2014.
384 Take, W. A., Bolton, M. D., Wong, P. C. P. and Yeung, F. J.: Evaluation of landslide triggering
385 mechanisms in model fill slopes, Landslides, 1(3), 173–184, doi:10.1007/s10346-004-0025-1, 2004.
386 Yin, Y., Li, B., Wang, W., Zhan, L., Xue, Q., Gao, Y. and Zhang, N.: Mechanism of the December 2015
387 Catastrophic Landslide at the Shenzhen Landfill and Controlling Geotechnical Risks of Urbanization,
388 Engineering, 2(2), 230–249, doi:10.1016/J.ENG.2016.02.005, 2016.
389 Zhang, Y., Qi, M. and Ma, H.: Slope instability and its control in Shenzhen City, Chinese J. Rock Mech.
390 Eng., S2 (in Chinese), 2006.
391 Zou, D. H.: Exploring a Waste Dump Site Failure–Possible Causes and Prevention Measures, Int. J.
392 Geohazards Environ., 2(1), 25–33, 2016.
393